Nuclear Instruments and Methods in Physics Research A 1065 (2024) 169494

Contents lists available at ScienceDirect

Nuclear Inst. and Methods in Physics Research, A

journal homepage: www.elsevier.com/locate/nima

Full Length Article

X-ray characterization of a bulk resistive MICROMEGAS operating at low gas pressure

A. Foresi [b,a,*], G. Antonelli [a], C. Avanzini [a], G. Balestri [a], G. Bigongiari [b,a], R. Carosi [a], F. Frasconi [a], P. Maestro [b,a], C. Magazzù [a], M. Massa [a], A. Moggi [a], F. Morsani [a], F. Pilo [a], G. Terreni [a]

[a] INFN Sezione di Pisa, Polo Fibonacci, Largo B. Pontecorvo 3–56127 Pisa, Italy
[b] Department of Physical Sciences, Earth and Environment, University of Siena, via Roma 56, 53100 Siena, Italy

ARTICLE INFO

Keywords:
Gas detector
MICROMEGAS
Low pressure regime
X-ray

ABSTRACT

In the last decades, interest has grown in the development of detectors that can accurately measure energy and track of low-energy (1–100 keV) charged particles. In this paper we present our effort to construct a resistive MICROMEGAS detector with a wide amplification gap (192 μm), to achieve high gain with a low discharge probability, even when operating with a low-pressure gas down to 50 mbar. The detector response (gain, energy resolution, relative primary charge collection efficiency) to X-rays from a ^{55}Fe source was measured under different operating conditions of amplification and drift fields, gas pressure and gas mixture composition. The results obtained and their temporal stability demonstrate that the detector can be used for the measurement of low-energy radiation with good energy resolution.

1. Introduction

In the last decades, interest in the development of detectors sensitive to low-energy ionizing radiation has grown significantly. The fields of application for such detectors are constantly expanding, encompassing diverse areas such as microdosimetry [1], direct Dark Matter detection [2,3], plasma monitoring [4] and the study of planetary magnetosphere dynamics [5–7]. In this latter context, there exists a pressing need for detectors capable of precisely sensing ions with energies in the keV range, accurately measuring their energy, and simultaneously providing a reconstruction of their trajectories [8]. Instruments flown to date in solar physics and planetary exploration missions [9–11] are based on solid-state detectors and microchannel plates and have limitations such as: reduced energy range in which they can operate; small field of view and acceptance; poor angular resolution (> 10°), especially at low energies; only 1D imaging capability due to the use of slit windows and one-dimensional detector arrays.

To overcome these limitations, our research group is actively developing a specialized detector designed to detect ions with energies from 1 to 100 keV, with a large field of view and improved imaging capability [12,13]. Our detector is based on the MICRO-MEsh GAseous Structure (MICROMEGAS - MM) technology [14], a Micro Pattern Gas Detector widely utilized in high-energy physics experiments. Under normal temperature and pressure (NTP) conditions, it has an energy resolution of 25-30 % Full Width Half Maximum (FWHM) for particles with energies in the few keV range. However, ions in this energy range only leave traces of a few tens of micrometers as they pass through the gas, and then their trajectory cannot be reconstructed. A significant improvement can be achieved by operating this detector at an internal gas pressure of tens of millibars, while maintaining comparable performance levels. That allows the ion track to stretch to the order of millimeters, facilitating proper track reconstruction with the typical pitch of the readout electrodes (100-200 μm).

The aim of the experimental work described in this paper is to demonstrate that the MM, suitably adapted, can operate at low pressure with stable performance and reasonably high primary charge amplification. The MM detector is described in detail in Section 2, while Section 3 focuses on the experimental setup, including the gas distribution system, slow control and DAQ chains. Section 4 presents a characterization of the response of the MM irradiated with X-rays from a ^{55}Fe source when its operating point is varied by changing the applied electric fields, the composition of the gas mixture and the gas pressure in the range of 500 mbar down to a minimum of 50 mbar.

2. Detector characteristics

All the experimental results presented in this report have been obtained using a resistive MM based on the bulk technology [15]. This

* Corresponding author.
E-mail address: andrea.foresi@pi.infn.it (A. Foresi).

https://doi.org/10.1016/j.nima.2024.169494
Received 2 March 2024; Received in revised form 12 May 2024; Accepted 3 June 2024
Available online 6 June 2024

design ensures stable and uniform working conditions by suspending the mesh using insulating spacers (pillars) printed on top of the anode plane. The anode consists of a thin sputtered layer of high-resistivity diamond-like carbon (DLC) to suppress electrical discharges and prevent localized drops in the potential difference in the presence of high charge densities. The height of the pillars, set during manufacture, defines the thickness of the avalanche volume between the mesh and the anode, which must be chosen in the design phase in order to obtain optimum charge amplification without approaching the breakdown voltage limit in the gas pressure range for which the detector is intended to operate.

Our MM prototype has been equipped with a mechanical support structure and a custom-designed gas distribution system in order to operate at low pressure. A very low-noise high-voltage power supply and charge-sensitive preamplifier were developed specifically to ensure high signal-to-noise ratio (SNR).

2.1. Main MICROMEGAS characteristics

The MM PCB, equipped with the micro-mesh bulk and the DLC layer has been designed and fabricated by the CERN EP-DT Micro Pattern Technology (MPT) Workshop. While sharing many common characteristics with the standard MM kit used for the R&D of larger experiments, like the muon system of ATLAS [16], our detector prototype features a larger amplification gap of 192 μm instead of the usual 128 μm. Here are reported the main characteristics of our MM prototype:

- 400 line-per-inch nickel woven wire mesh (wire diameter: 18 μm);
- the nominal avalanche gap height was specified to be 192 μm by the manufacturer;
- single DLC layer with a resistivity of about 50 MΩ/sq;
- read-out plane consisting of 256 strips in X and 256 strips in Y direction (400 μm-pitch);
- active area of 102.4 $\times$102.4 mm^2, as from the CAD design provided by the manufacturer.

2.2. Mechanical support frame

In the design of the detector mechanical frame, the main requirement to be fulfilled was to ensure excellent gas tightness with a low leak rate, thus reducing the contamination of atmospheric oxygen and humidity. In [17], the impact of oxygen contamination on primary electron loss in the drift region was assessed under normal pressure conditions. Remarkably, even a tiny oxygen concentration of 0.01% in the gas mixture resulted in a notable 10 % reduction in primary electron count, particularly evident under very low drift field strengths. While corresponding measurements at low pressure remain unavailable, we prudently adhere to the same contamination threshold as a requirement for our design. Additionally the mechanical frame must sustain a differential pressure of at least 1000 mbar without affecting the detector integrity and performance. At the same time the square section of the frame and the size of the fastening bolts was dictated by the PCB design, typically intended for operation at NTP.

In our design, the support frame (Fig. 1, 2) includes a full metallic frame consisting of a rear plate, a lateral frame, and a top cover that seals the gas box. The lateral frame has a height of 20 mm and the cathode is mounted on the inside of the MM top cover so that the drift volume is approximately 20 mm high. The thickness of the top cover, as well as the hole patterns and grooves on the outer top cover plate, result from the necessity to install the detector along a beam pipe using standard vacuum connections. The central hole allows for the insertion of a radioactive source and the passage of a particle beam.

With the aim of enhancing low pressure performance characteristics, the mechanical frame was designed with the following features:

- a 5 mm-thick aluminum reinforcement plate was glued on the back of the PCB;
- the lateral frame is composed of two parts: the lower part is a thin aluminum frame glued to the PCB top layer improving the flatness of the surface and then the sealing at the interface of the PCB and the lateral frame itself; an upper lateral frame made of stainless steel with welded gas pipes and Swagelok VCR connectors;
- indium wire sealing between the two components of the lateral frame and between the lateral frame and the top cover. According to our tests, using indium wire achieved a much better seal than the results obtained with polymeric O-rings;
- Swagelok VCR diaphragm valves are installed at both the gas inlet and outlet, allowing for a complete separation of the detector from the gas system so that its performance can be evaluated under static conditions.

2.3. Cathode

The MM cathode (Fig. 3) was fabricated as a PCB in the form of a single square pad with a lateral size of 100 mm. Arlon 35N was chosen as the PCB substrate due to its vacuum compatibility. The center of the pad features a 2 mm through hole, and a 10 μm-thick stainless steel pinhole with a diameter of 9.5 mm is affixed on top of it, enabling the passage of particles through a central hole with a diameter of 5 μm. Special attention was given to the assembly of the cathode. It was attached to the inner face of the top cover using a low outgassing structural adhesive, which provides an effective seal even on low adhesive surfaces and under harsh environmental conditions.

The overall sealing performance of the detector frame was tested using a helium leak detector according to the test procedure detailed in [18], yielding a value below 10^{-6} mbar l/s.

2.4. Support electronics

The high-voltage power supply scheme involves setting the mesh to ground, the anode to a positive amplifying voltage, and the cathode to a negative voltage value to ensure an adequate drift field. The mesh is grounded through a 100 MΩ resistor, connected in series with a parallel arrangement of a 10 MΩ resistor and a 4.7 nF capacitor, serving as an RC filter. This filter is then connected in series with a picoammeter, which is utilized for measuring the mesh current. The detector frame and supporting mechanics are kept at the same potential of the mesh via cable connections. All the read-out strips are terminated to the system ground through 1 MΩ resistors to avoid noise injection on the mesh.

According to this configuration, the main components of the MM support electronics include a 2-channel HV power supply for the cathode and the anode, and a charge-sensitive preamplifier connected to the mesh, properly decoupled via a capacitance.

The high capacitance between anode strips and mesh (851 pF) resulted in specific requirements for the HV power system and the front-end chain of the mesh electrode.

2.4.1. High voltage supply

Due to the high capacitance of MM, the very low-frequency noise produced by the common commercial power supply generates noise that overlaps with the mesh signal and deteriorates the SNR of the detector.

Following our directions, a custom electronics manufacturer was able to provide an evaluation prototype that works at very low noise, the characteristics of which, for both the negative and positive channels, are summarized in Table 1.

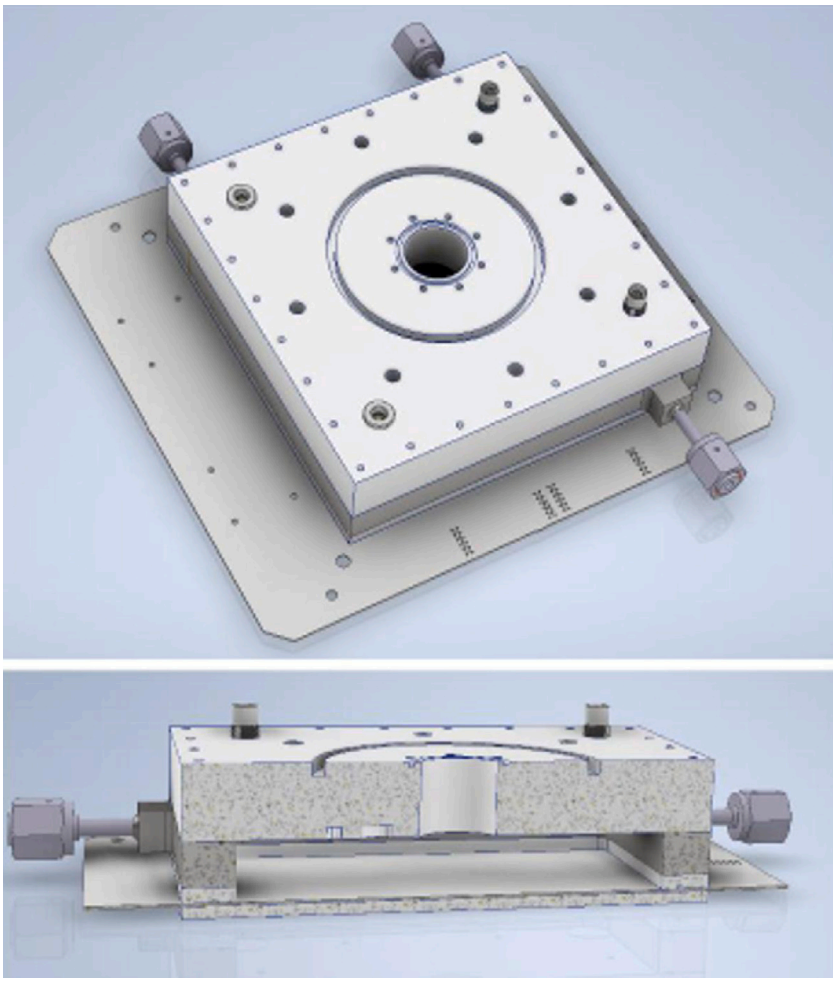

Fig. 1. 3D and cross-section view of the detector mechanical support frame.

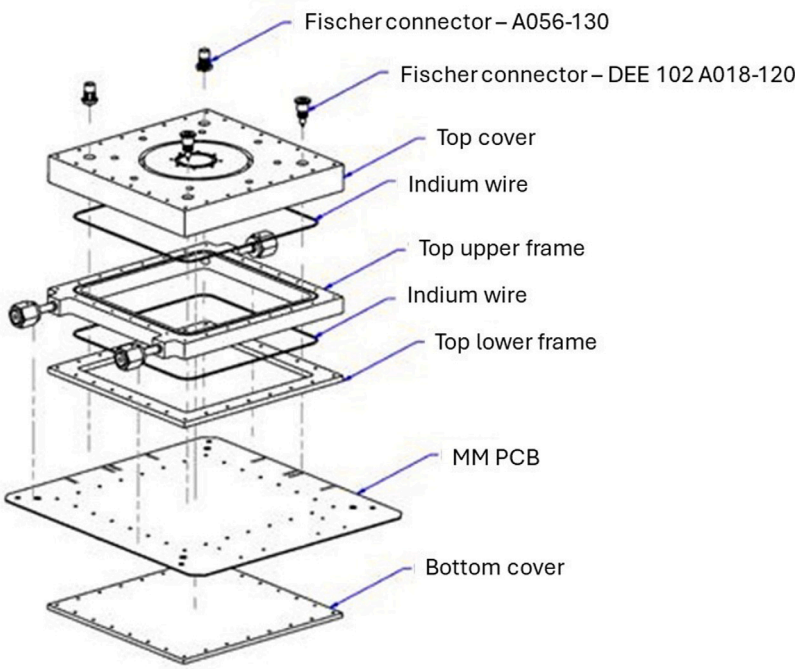

Fig. 2. Exploded view of the MM mechanical support frame.

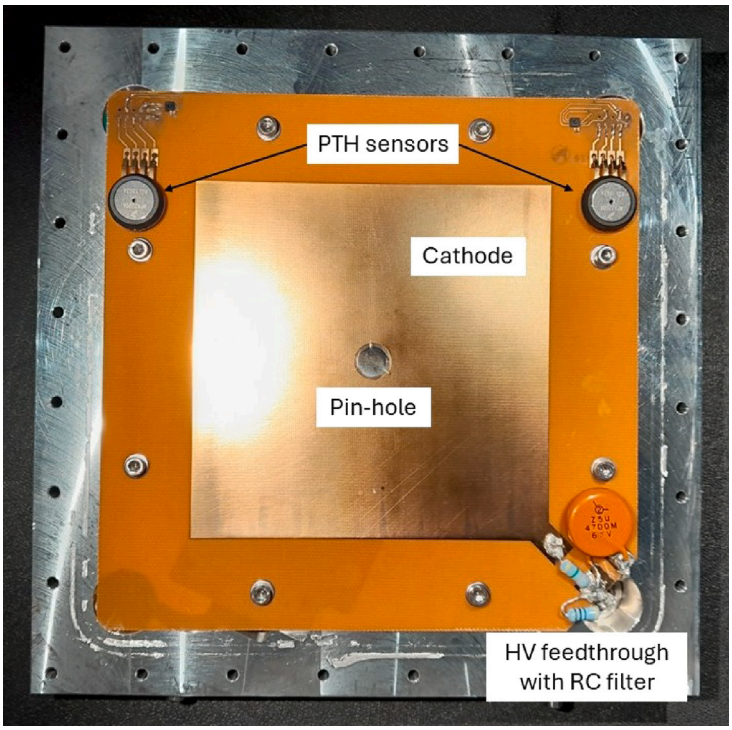

Fig. 3. Top view of the MM cathode showing the 5 μm-pinhole, the PCB the pressure-temperature-humidity sensors, and the HV feedthrough with the RC filter.

Table 1
Main features of the custom low-noise HV power supply developed for our MM detector. Above 10 Hv the voltage ripple is significantly suppressed compared to standard commercial power supplies.

Output Voltages	0-600 V in 0.1 V steps, one positive and one negative channel
Max. Output Current	500 μA
Voltage Ripple	< 5 mVpp between 0.1 Hz and 10 Hz, < 200 μVpp above 10 Hz
Thermal Drift	<100 ppm/°C
Power Supply	230 V AC

Table 2
Main characteristics of the custom CSP. The characterization was performed observing noise signal in a bandwidth of 10 Hz - 20 MHz and using a capacitor of 825 pF in series to the CSP input to emulate the detector capacitance. The gain estimation was done injecting in the CSP a charge of 13.6 fC.

Gain	7.35 mV/fC
ENC	0.650 fC
Rise time	340 ns
Fall time	380 μs
Dynamic range	3-225 fC

2.4.2. Micromesh front-end chain

In our MM detector the energy measurement is provided by a Charge-Sensitive Preamplifier (CSP) which amplifies the signals induced on the mesh electrode by the electron avalanches. The increased size of the avalanche gap leads to changes in the input capacitance of the CSP which in turn affect the SNR and consequently the detector energy resolution. We have designed a custom device to fulfill our specific requirements, specifically aiming for a low Equivalent Noise Charge (ENC) to minimize the lower energy threshold, while consistently ensuring optimal charge amplification across the widest possible bandwidth [19].

The CSP is capable of detecting a charge buildup of at least 4.8 fC (3×10^4 e$^-$), which corresponds to a ionization energy deposit of 1 keV with a MM gain of 10^3. The CSP boasts several key features, summarized in Table 2, including an exceptionally low ENC of 0.650 fC, corresponding to a SNR > 5.

In the low-pressure regime, where achieving high gain values is challenging, the detector's SNR deteriorates, rendering its output more susceptible to environmental noise, especially microphonic noise. To mitigate this, a high-pass filter (CR, with C = 268 nF and R = 50 Ω) has been incorporated in series with the CSP output, effectively attenuating low-frequency components.

3. Experimental setup

A dedicated experimental test bench was designed and installed at the INFN Pisa laboratories (see Fig. 4(a)). In order to study the behavior of MM under low pressure working conditions, the experimental setup was complemented with a monitoring system that continuously records the most relevant control parameters, such as gas temperature and pressure, mesh current and ambient temperature.

Regarding the interface between the X-ray source and the detector, a special stainless steel collimator (shown in Fig. 4(b)) was developed to address the need for frequent source removal to evaluate background currents. The X-ray source is inserted into a threaded rod, which can be screwed into a cylindrical adapter fitted with a Kapton window on the MM's top cover, ensuring the detector's seal with a Viton O-ring. Removal of the collimator from the detector does not necessitate any modifications to the detector's operating conditions. This approach also avoids any alterations in the source-to-MM distance, which could otherwise affect the number of X-rays reaching the gas cell due to changes in the system's angular aperture.

Below are summarized the main characteristics of the principal components of the test bench.

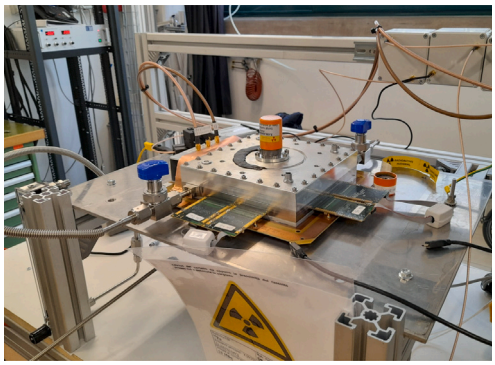

(a)

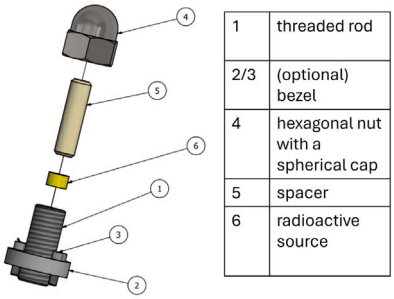

1	threaded rod
2/3	(optional) bezel
4	hexagonal nut with a spherical cap
5	spacer
6	radioactive source

(b)

Fig. 4. (a) The MICROMEGAS installed in the INFN Pisa test bench. (b) The custom collimator developed to install the ^{55}Fe X-ray source on the MM.

3.1. Gas distribution system

The detector gas mixture, selected from the most commonly used and well-known mixtures for MM operation at NTP, consists of Ar/CO_2 in 93 % and 7 % volume ratio. The gas distribution system must ensure an ultra-high-purity gas flux with pressure stability on the order of tenths of a mbar over extended periods of time.

Our gas distribution system (Fig. 5(a)) meets these requirements through the following components:

- high-precision, metal-sealed Mass Flow Controllers (MFCs) remotely controlled by a dedicated readout and setpoint device. Each MFC can be individually reprogrammed with the calibration of a different gas, allowing for adjustments to the gas mixing percentages;
- a MFC setpoint controller with fine regulation of the gas flux, capable of adjusting down to a few tenths of cc/min. The flux rate must be independent of downstream pressure and stable over time;
- a gas mixing volume to ensure homogeneous gas distribution;
- an additional gas reservoir buffer connected to the detector outlet, increasing the overall low-pressure volume and acting as a buffer between the MM and the pressure regulator. This configuration enhances stability by increasing the reaction time required to compensate for any pressure variations;
- a high-precision back pressure regulator based on a flexible diaphragm as its only moving part, providing frictionless motion and more stable operation;
- stainless steel pipes and Swagelok connections for all non-critical system components, with Swagelok VCR connections for low-pressure volume;
- inline particulate filters (FITOK FTSS-FL4-2-F2, nominal pore sizes: 2 μm) capable of filtering particles down to a few micrometers in size.

During all the detector characterization test campaign a continuous renewal of the sensitive gas with a flux of 40 cc/min allowed to keep the oxygen contamination below the requested 0.01 % level.

3.2. Detector parameters monitoring and control

Sensors to monitor Pressure, Temperature, and Humidity (PTH) are installed both inside, directly on the same PCB used for the cathode (Fig. 3), and outside the MM to monitor the detector's inner gas and the laboratory conditions. All the sensor readouts communicate with the database server; data from the trigger rate meter and mesh current picoammeter are also stored in the same database, completing the continuous monitoring of the detector status.

The MM temperature control is realized using four Peltier cells coupled to its own cooler fan, installed on the MM rear plate (shown in Fig. 5(b)). This system guarantees a maximum temperature difference of 4 °C between the environment and the gas inside the cell. gas inside the cell, even in the hottest season. During data collection, the temperature in the gas cell was monitored by a sensor with a resolution of 0.1 °C.

3.3. Low-voltage and electrical noise reduction

Low voltages for all the active systems of the detector, such as PTH sensors and CSP, are supplied by a unique low-noise, three outputs, commercial desktop power supply. The integration of these components, along with the implementation of return potential connections to the detector frame and support mechanics, has enabled us to achieve the optimal electrical configuration for noise reduction.

An essential step in the noise filtering process involved filtering out frequencies below 10 kHz from the amplified signal. For this purpose, the use of the "choke" technique, particularly effective on ground and power cables (where each cable is wound around a ferrite toroidal core), precise cabling with 50 Ω shielded coaxial cables and SMA connectors and the inclusion of a high-pass filter in the mesh read-out chain, were crucial.

3.4. Trigger and DAQ system

The trigger logic, whose scheme is shown in Fig. 6, is implemented using NIM modules housed in a NIM crate.

The CSP output signals are distributed using a LeCroy 428F fan-in/fan-out module. One of the outputs is directed to the CAEN N844 Low Threshold Discriminator (LTD), which enables threshold adjustment down to few millivolts, facilitating the digitization of very low amplitude negative signals. Incorporating an analog 9^{th}-order Chebyshev low-pass filter with a cutoff frequency of 106 kHz significantly enhances the signal to noise discrimination. As depicted in Fig. 7, the spectrum acquired with the analog low pass filter demonstrates a substantial separation between the particle signals and the noise but worsens the energy resolution. Consequently, the filter is not directly employed in the DAQ chain, but only to improve the trigger capability.

The LTD output signals are sent to a CAEN N93B dual timer. This timer stretches the output pulses to a fixed width of 100 ns, stabilizing their temporal duration and produces a 50 μs 'trigger holdoff' to mitigate issues related to double-counting events occurring too closely in time. Subsequently, the trigger signals from the dual timer are routed back to another port on the fan-out module and distributed to the DAQ instruments.

The main DAQ instrument is a computer-controlled DT5725SB CAEN digitizer, with a nominal 14-bit vertical resolution, which samples the CSP analog waveforms at a frequency of 250 MS/s for offline

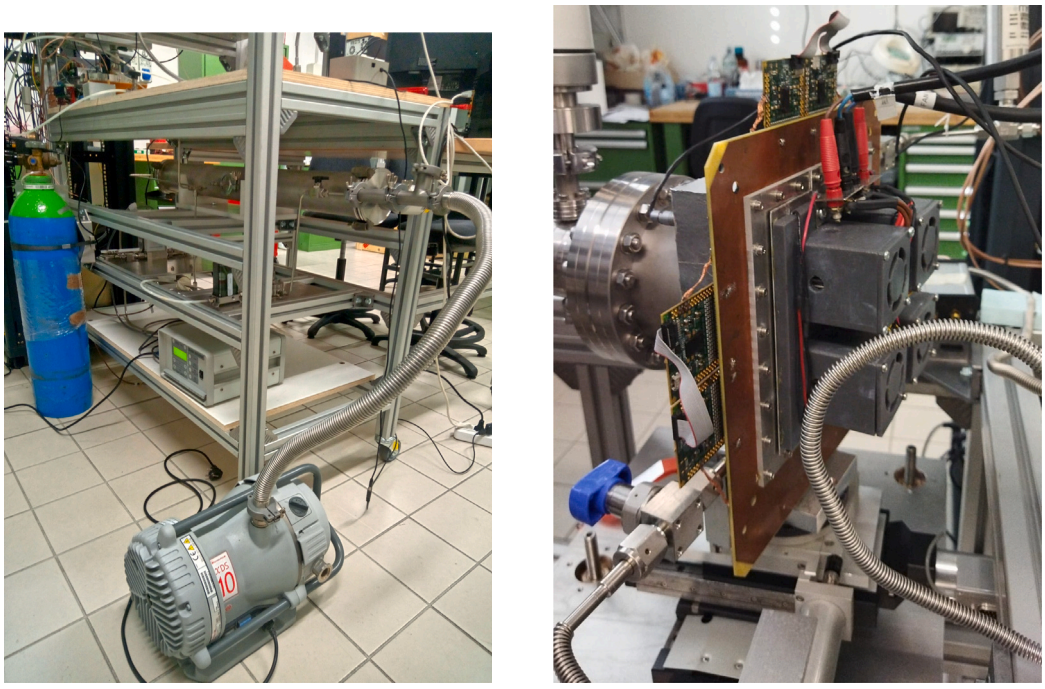

(a) (b)

Fig. 5. (a) The gas distribution system. (b) The temperature controller system made of four Peltier plates, coupled to its own cooling fan, attached to the back of the MM.

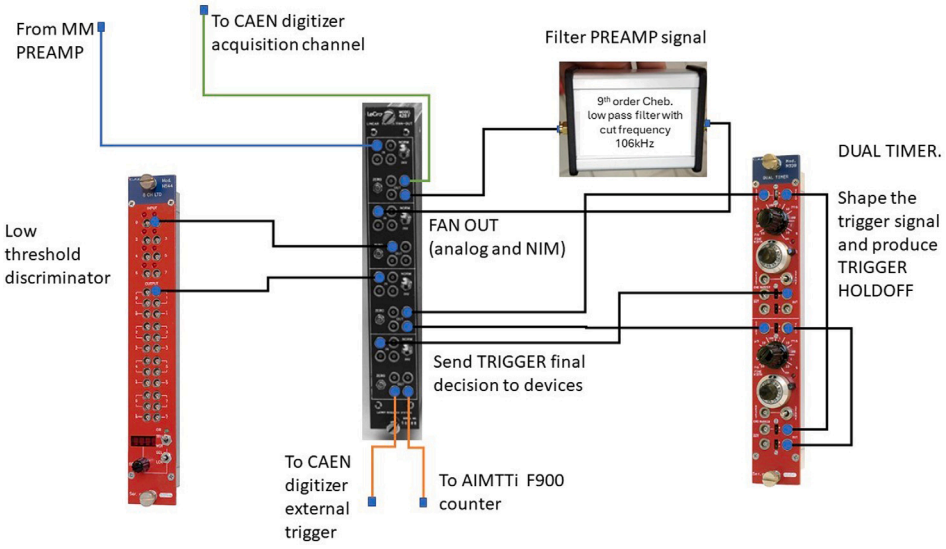

Fig. 6. A scheme of the connection between NIM logical modules and the 9th order Chebyshev filter. The mesh signals are distributed to the DAQ instruments and to the filter. The threshold discriminator is applied on the filtered signals and then a Dual timer module is used to create an hold off window to avoid double counting and the trigger signal. The trigger is finally distributed to the DAQ instrumentation and to a counter.

reconstruction and analysis. For precise trigger rate measurements a Model TTi TF930 30 GHz counter is also feed with the NIM trigger signal previously described. The mesh current I is measured using a Keithley-2410 picoammeter directly connected between the mesh output and the system ground.

4. Experimental measurements

The detector was characterized using a ^{55}Fe radioactive source with an activity of 10 MBq which emits X-ray photons at 5.90 keV and 6.49 keV by electron capture. Photoelectrons resulting from X-ray absorption ionize the gas by producing electron–ion pairs. The electrons drift toward the mesh and give rise to an avalanche in the gap region between the mesh and the anode, where the electric field is intense (tens of kV/cm). The charge of the avalanche induces electrical signals on the mesh and anode electrodes respectively.

In this report, only the measurements derived from the mesh signal analysis were considered.

4.1. Detector gain

The detector multiplication factor M, or gain, is defined as the ratio between the collected charge N_s and the primary ionization charge N_e for each X-ray interaction [20].

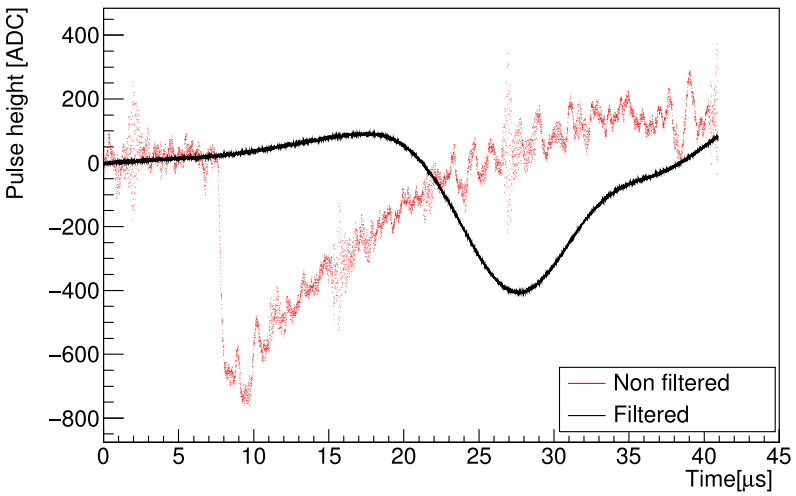

(a)

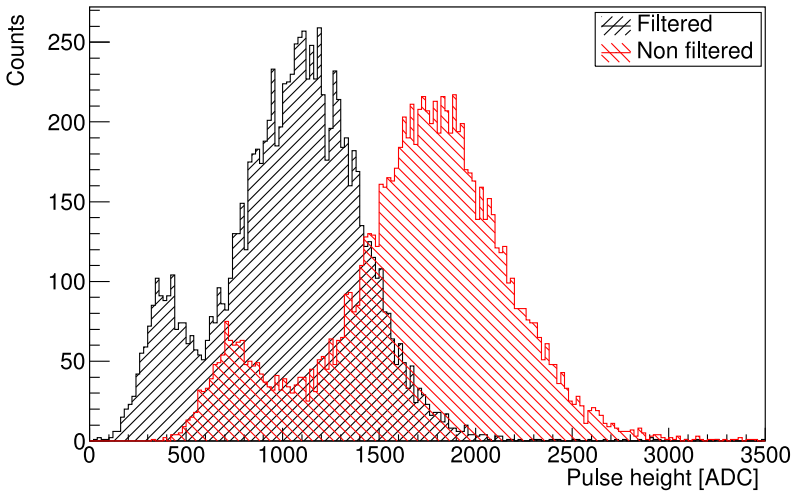

(b)

Fig. 7. Examples of signals obtained by irradiating the MM with a beam of He ions at 5 keV (a) and corresponding energy distributions (b) with (black line) and without (red line) applying the 9th order Chebyshev low pass filter. Filtering the mesh signal increases the SNR increase from 2.38 to 2.75, but degrades the resolution of the main peak from 46% to 63%. The SNR is here estimated as the ratio of the signal to the noise peak position.

N_s is estimated by measuring the signal current I_s and the rate R_s of X-rays detected according to the formula:

$$N_s = \frac{I_s}{e\,R_s} \tag{1}$$

where e is the elementary charge, I_s is estimated as the difference between the mesh current measured when the detector is irradiated and the background current without the X-ray source and, similarly, the trigger rate R_s is given by the difference in the count rate with and without the source.

The number of primary electrons N_e generated when an X-ray interacts with the gaseous medium can be calculated as:

$$N_e = \frac{E_\gamma}{W} \tag{2}$$

where E_γ is the energy of the photon and W the average energy to produce an electron–ion pair in the gas. Given $W = 26.3$ eV for Ar [21] and an average $E_\gamma = 5.9$ keV for X-ray emission from ^{55}Fe decays, we get $N_e = 223$.

However, for an accurate evaluation of N_e several effects must be considered. First, the X-ray source is not monochromatic. Electron-capture decays of ^{55}Fe nuclei produce Mn K-shell X-photons at 5.90 keV and 6.49 keV with emission probabilities of 24.4% and 2.86%, respectively [22]. In addition, a significant fraction of the energy released by the interacting photons can escape from the sensitive volume of the detector through the emission of the characteristic Ar fluorescence X-rays at 2.9 keV, which have a longer absorption length than X-rays of higher energy [23]. The detection efficiency depends on the energy of the photons and decreases at low gas densities, at which the probability of escape is therefore higher.

A Monte Carlo simulation of the MM detector based on Geant4 [24], Garfield [25] and Degrad [26] was developed to evaluate N_e at different gas pressures. An example of the distribution of N_e obtained from the simulation is shown in Fig. 8, where the Ar escape peak is clearly visible to the left of the main peak produced by the X-photons of energy 5.90 keV emitted by the ^{55}Fe source. Each peak i is fit to a Gaussian to obtain the mean value of n_{ei} and the integral A_i of the curve. The simulation was carried out separately for the two ^{55}Fe emissions considered (5.90 keV and 6.49 keV) at all the pressure values studied. The average value of N_e is calculated as $N_e = \sum_i n_{ei} P_i$ where P_i is the ratio of A_i to the total integral of the distribution, weighted for

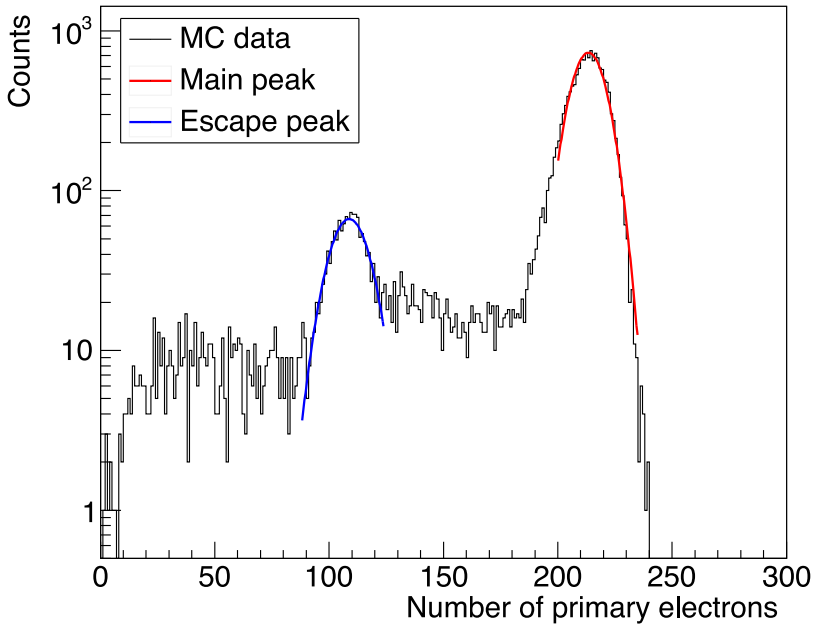

Fig. 8. Distribution of primary electrons N_e produced by the 5.9 keV ^{55}Fe X-ray photons in a gas mixture of Ar/CO_2 (93:7) at a pressure of 50 mbar.

Table 3
N_e for different gas pressures. The third column shows the percentage difference from the estimate (N_e = 223) calculated considering only the 5.9 keV X-ray line and neglecting the Ar escape peak.

Pressure [mbar]	N_e	Difference [%]
50	204 ± 28	8.6 ± 1.2
75	208 ± 23	6.87 ± 0.76
100	210 ± 39	5.8 ± 1.1
150	211 ± 38	5.5 ± 1.0
500	215 ± 29	3.83 ± 0.51

Table 4
The anode voltage and cathode voltages set for each pressure value.

Gas pressure [mbar]	Anode voltage [V]	Cathode voltage interval [V]
500	445	200, 300, 400, 500
150	310	50, 100, 200
100	280	20, 30, 50, 75, 100, 200, 300
50	253	20, 30, 40, 50, 75, 100, 125, 150

the emission probabilities of the X-ray lines. The results of the factor N_e at different gas pressures are shown in Table 3 and compared with the rough estimate that does not take into account the escape peaks and the gas pressure. Percentage differences range from a low 3.0% at 500 mbar to a high of 6.8% at 50 mbar.

4.2. Pulse height spectrum

The waveforms recorded by the digitizer, examples of which are shown in Fig. 9 for two different MM operating conditions, are converted into ROOT [27] files and analyzed offline with custom C++ codes. The pulse height is proportional to the total charge released in the detector by the interacting X-ray. To extract the pulse height, each waveform is fitted to the function:

$$f(t) = C\left[\frac{1}{\exp\left(\frac{t-\mu}{\tau_f}\right)+1} - 1\right]\exp\left(\frac{2\mu - t}{\tau_r}\right) \quad (3)$$

where the Fermi–Dirac (FD) term (between square brackets) models the fast ion collection on the mesh electrode [28] and the exponential tail describes the discharge of the amplifier. The function (3) depends on four parameters: a normalization constant C; a shift parameter μ related to the trigger delay time; the time constant τ_f of the FD; the decay constant τ_r of the exponential function.

Two pulse height distributions are presented in Fig. 10 where the highest peak in the spectra is the sum of the 5.90 keV and 6.49 keV lines of the ^{55}Fe source, while the escape peak is evident at lower signal amplitudes. A gaussian fit to the main peak in the distribution is performed to estimate the energy resolution of the detector, calculated as the ratio of the FWHM to the mean value.

5. Detector characterization

The entire data collection campaign took several months during which the detector was constantly fed with HV values close to the operational settings and the gas mixture continuously renewed with a constant flux of 40 cc/min. The gas was maintained at a constant pressure within 0.5 mbar and at a temperature range between 19.5 and 21.5 °C.

The instrument response was studied at 5 different gas pressure values: 500, 150, 100, 75, and 50 mbar. For each pressure value, measurements were performed by varying the cathode voltage (thus changing the MM drift electric field), the anode voltage (thus changing the MM avalanche electric field), and the fraction of CO_2 in the gas mixture. After two days of stabilization for each gas pressure setting, measurements were repeated at least twice on two different days to account for possible long-term variations.

5.1. Varying the cathode voltage

The variation of the number N_s of electrons per X-ray as a function of cathode voltage was studied. For each pressure value, the anode voltage was chosen in order to obtain a high SNR while avoiding discharge phenomena during electron multiplication in the avalanche.

For each set of measurements obtained by varying the cathode voltage at a given pressure and fixed anode voltage (Table 4), the value of

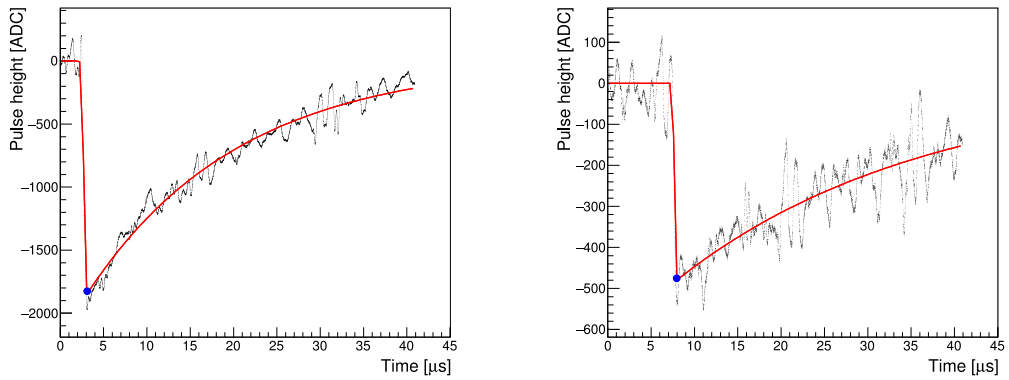

Fig. 9. Typical digitized waveforms acquired when an ^{55}Fe X-ray is detected by the MM with a gas pressure of 500 mbar (a) and 50 mbar (b). The red line represents the fitted function (3). An estimate of the collected charge is given by the height of the fitted peak, indicated by the blue dot.

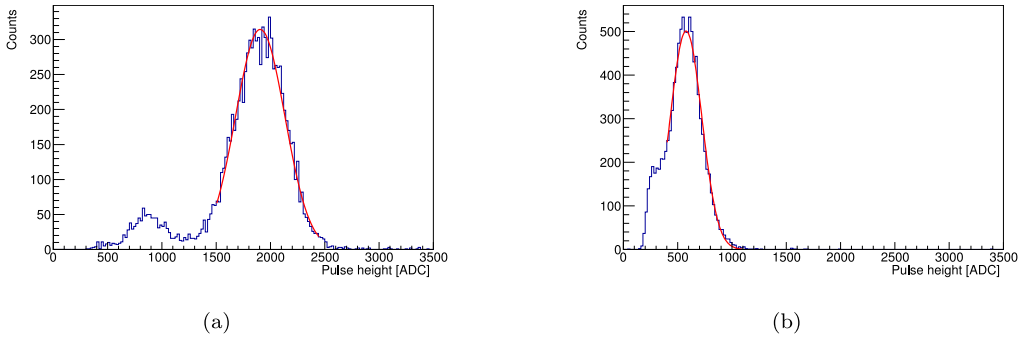

Fig. 10. Pulse height distribution obtained irradiating the MM detector with X-rays from a ^{55}Fe source, under different gas pressure conditions: 500 mbar (a) and 50 mbar (b), respectively. It can be seen that at low pressure, the escape peak is not evident anymore.

N_s is normalized to the maximum measured value. This ratio indicates how the relative efficiency of primary charge collection varies as a function of the ratio between the drift electric field and the avalanche electric field, as shown in Fig. 11. The drift (avalanche) electric field is defined as the ratio of voltage difference over the distance between the cathode (anode) and the mesh.

At pressure values between 50 e 150 mbar, the highest relative collection efficiency is reached for a drift-to-avalanche electric field ratio of about 0.0013. At low values of the drift electric field, the primary charges are not sufficiently accelerated to reach the mesh and undergo recombination with the gas, which causes a decrease in the collection efficiency. At high values of the drift electric field, however, the relative efficiency decreases indicating a loss of the mesh transparency due to the absorption of primary electrons by the mesh itself [29]. This behavior differs significantly from that measured at NTP, where the decrease starts at much higher values of the drift-to-avalanche electric field ratio, around 0.025 [29]. This is consistent with our measurements at 500 mbar which show a flatter mesh transparency extending to higher values of the ratio.

5.2. Varying the anode voltage

The multiplication factor M of the detector depends on the electric field between the mesh and the anode plane, which can be set by changing the anode voltage. Gain calibrations were performed as a function of anode voltage to determine, for each pressure value, the range of electric field intensity at which the MM can operate without entering the region of limited proportionality or discharge.

The measured number N_s of electrons per X-ray is shown in Fig. 12 as a function of the anode voltage. The multiplication factor M, calculated as explained in 4.1, is shown in Fig. 13. For each set of measurements at a given gas pressure value, the cathode voltage was set to a fixed value, close to the maximum of Fig. 11. The M factor increases exponentially with increasing anode voltage at all gas pressures. However we notice that as the gas pressure decreases, the average gain decreases and the anode voltage range in which the MM can be operated narrows considerably. At 50 mbar, a change of only a few volts brings the MM close to the discharge regime.

The MM gain stability was evaluated over an operating interval of one year. As an example, Fig. 14 shows the comparison between the measurements taken in 2022 and 2023.

The energy resolution of the MM is presented in Fig. 15 for all the pressure and anode voltage settings. It is calculated as the ratio of the FWHM to the mean value of the Gaussian fit to the pulse height distribution (Fig. 10). At 500 mbar, the energy resolution is nearly constant at 30% over the entire anode voltage range. At lower pressures the energy resolution deteriorates rapidly as the anode voltage increases. This suggests a potential shift in the regime of electronic avalanche formation, where the contribution to the total number of electrons by secondary avalanches becomes significant [30]. Nevertheless, by selecting the appropriate operating voltage, energy resolutions of 28% at 150 mbar, ~45% at 100 mbar and 75 mbar, 60% at 50 mbar can be achieved.

5.3. Varying the co_2 fraction in the gas mixture

In all previous measurements, an Ar/CO_2 gas mixture in 93/7 fractions was used. The operation of the MM was also studied with

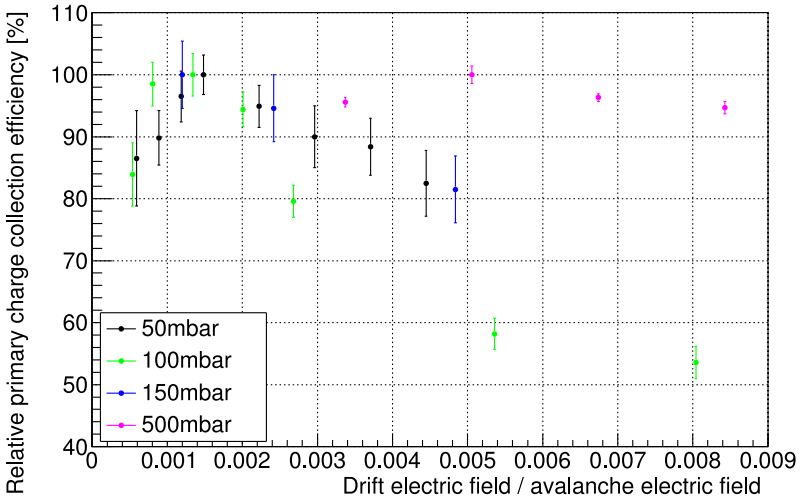

Fig. 11. Relative primary charge collection efficiency as a function of the drift-to-avalanche electric field ratio at different gas pressures.

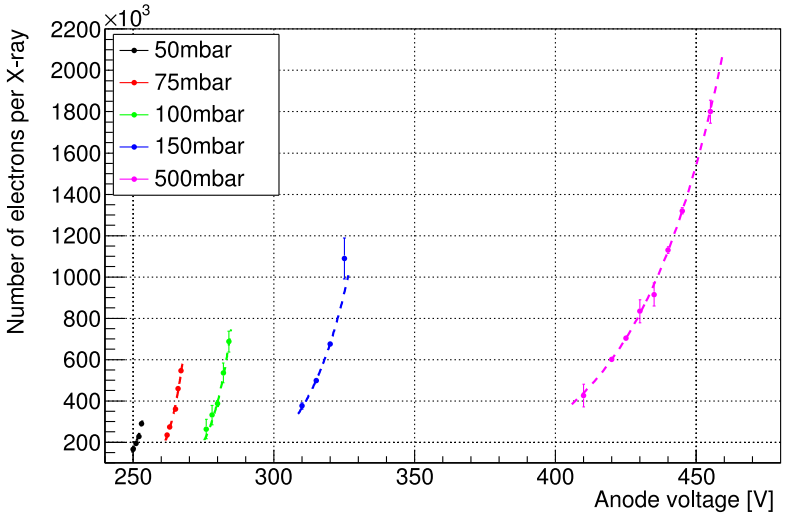

Fig. 12. Number of electrons N_s per single X-ray as a function of the anode voltage for different gas pressure values. Each data set is fitted to an exponential function indicated by the dashed line.

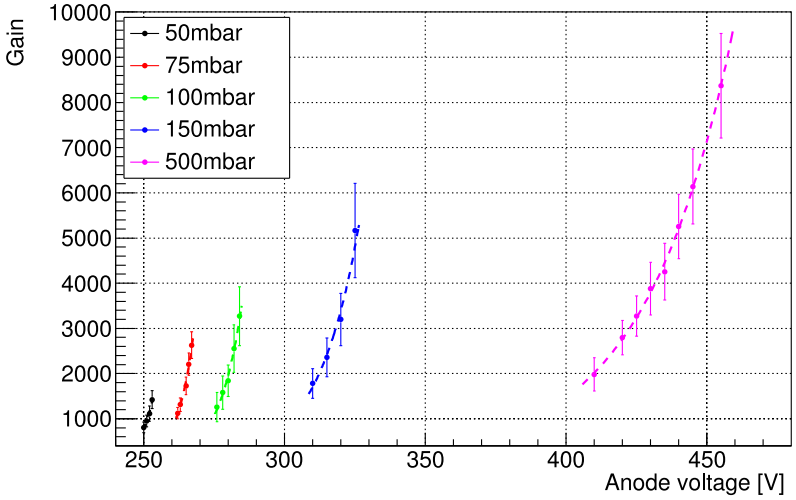

Fig. 13. Multiplication factor M as a function of the anode voltage for different gas pressure values. Each data set is fitted to an exponential function indicated by the dashed line.

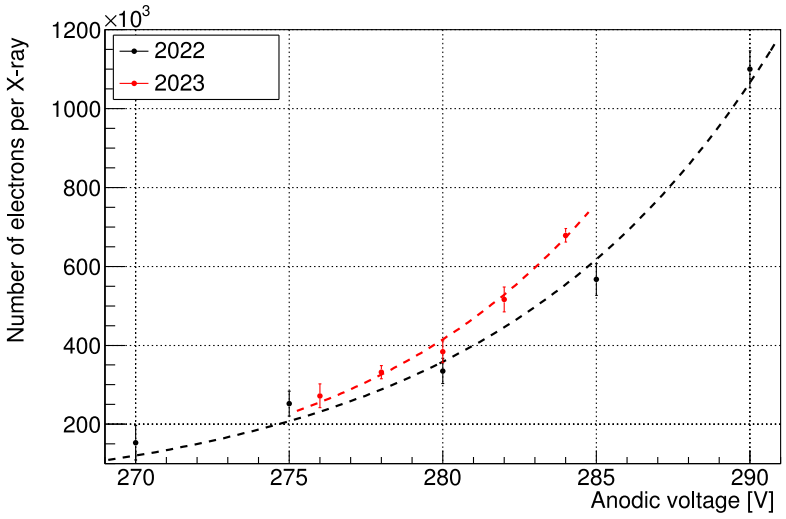

Fig. 14. Long-term stability of the number of electrons generated per single X-ray as a function of avalanche voltage at a pressure of 100 mbar. Two sets of data, taken at a distance of one year, in 2022 and 2023, are compared.

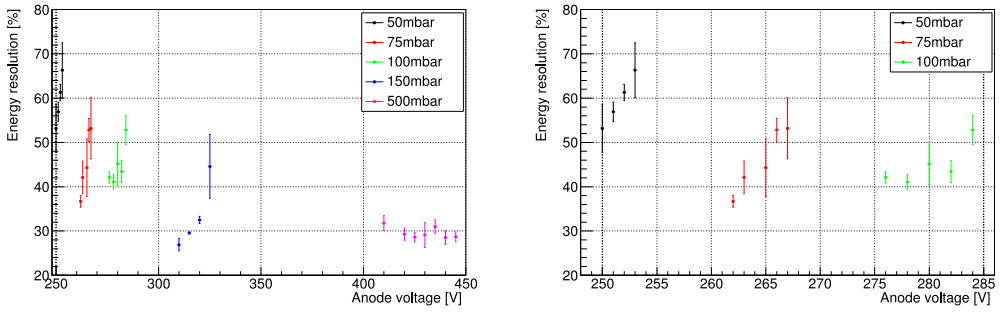

(a) (b)

Fig. 15. Energy resolution (FWHM) as a function of anode voltage at different gas pressure values (a). Figure (b) provides a closer view of the data sets obtained at pressures below 150 mbar, offering a detailed examination of this specific range.

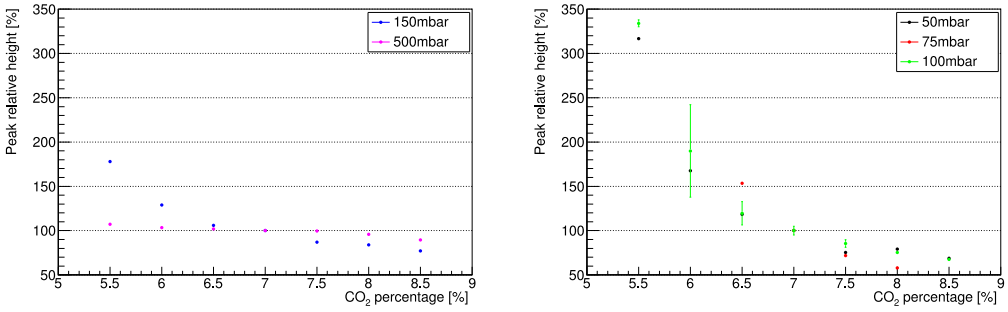

(a) (b)

Fig. 16. Average signal height of main peak of the ^{55}Fe X-ray spectrum normalized to the reference peak value (mixture with 7 % of CO_2) as a function of the fraction of CO_2 in the mixture for gas pressure values of 150 and 500 mbar (a) and 100, 75 and 50 mbar (b). An uncertainty of ±0.25% has to be considered on all the values of CO_2 relative percentages.

different fractions of Ar/CO_2 in the gas mixture. For each gas pressure value, pulse height spectra of the ^{55}Fe source were acquired by varying the CO_2 fraction in a range from 5.5 % to 8.5 %. The average signal height of the main peak in the spectra are normalized to the reference peak value (7 % of CO_2) and plotted as a function of the fraction of CO_2 in the mixture (Fig. 16). As expected, a reduction in the quencher fraction leads to an increase in the signal. At low pressures (below 150 mbar) this effect is enhanced by the increase of secondary ionization processes due to photon feedback in the avalanche. Furthermore, we find that the sensitivity of the MM response to small changes in the fraction of CO_2 in the mixture increases with decreasing pressure. This implies that the quencher fraction must be kept stable within 1 % to avoid large amplitude variations when MM operates at low gas pressures.

6. Conclusion

In this study, we have presented the results of an extensive test campaign aimed at characterizing the X-ray detection capabilities of a gas detector operating under low-pressure conditions.

The detector, a widened-gap resistive bulk MICROMEGAS, has been equipped with supporting mechanics and electronics that significantly improve its performance at low pressure. Our testing setup, using a ^{55}Fe radioactive source as the X-ray emitter, was designed to continuously monitor and control the operational parameters, ensuring reasonable reproducibility and temporal stability of the operating conditions. Furthermore, the data acquisition system and overall electronic configuration were calibrated to substantially improve the signal-to-noise ratio, without introducing signal distortion or bias that could jeopardize the detector accuracy.

All measurement procedures and offline data analyses were performed in a way that yielded simulation-free results, facilitating direct comparisons within the gas detector community.

Our detector has achieved an energy resolution comparable to that obtained under NTP conditions, down to at least 150 mbar [13]. However, this result involves trade-offs, including a narrow working range for the anode voltage, larger sensitivity to changes in the quencher fraction in the gas mixture, and susceptibility to fluctuations in density and temperature.

In the future, we expect that further progress can be achieved through a deeper understanding of the development of electronic avalanches at low pressure. That could be useful in optimizing the design of the avalanche volume, potentially allowing operation at pressures even below the 50 mbar limit.

Declaration of competing interest

The authors declare that they have no known competing financial interests or personal relationships that could have appeared to influence the work reported in this paper.

Data availability

Data will be made available on request.

Acknowledgments

This work is part of the Commissione Scientifica Nazionale 5 program SWEATERS funded by the Istituto Nazionale di Fisica Nucleare (INFN). We extend our gratitude to S. Bianucci and A. Soldani for their helpful contributions to the mechanical design, and to M. Ceccanti, A. Orsini, and A. Sardelli from INFN Sezione di Pisa for their exemplary technical expertise. Furthermore, we acknowledge our colleagues from the CERN RD51 collaboration for their significant contributions and constructive exchanges throughout the entire process of fine-tuning of our detectors.

References

[1] G. Parisi, F. Romano, G. Schettino, Microdosimetry for hadron therapy: A state of the art of detection technology, Front. Phys. 10 (2022) 1035956.
[2] D. Santos, et al., MIMAC: A micro-tpc matrix for directional detection of dark matter, J. Phys.: Conf. Ser. 309 (2011) 012014.
[3] Y. Tao, et al., Track length measurement of $^{19}F^{+}$ ions with the MIMAC directional dark matter detector prototype, Nucl. Instrum. Methods Phys. Res. A 985 (2021) 164569.
[4] V.I. Afanasyev, et al., Neutral particle analysis on ITER: Present status and prospects, Nucl. Instrum. Methods Phys. Res. A 621 (2010) 456–467.
[5] M. Gruntman, Energetic neutral atom imaging of space plasmas, Rev. Sci. Instrum. 68 (1997) 3617–3656.
[6] A.T.Y. Lui, D.J. Williams, E.C. Roelof, R.W. McEntire, D.G. Mitchell, First composition measurements of energetic neutral atoms, Geophys. Res. Lett. 23 (1996) 2641–2644.
[7] D.J. McComas, et al., The two wide-angle imaging neutral-atom spectrometers (TWINS) NASA mission-of-opportunity, Space Sci. Rev. 142 (2009) 157–231.
[8] N. Buzulukova, M.C. Fok, D. Sibeck, A. Keesee, H. Connor, M. Collier, R. DeMajistre, A. Glocer, K. Murphy, Global imaging of the Earth's magnetosphere with energetic neutral atom (ENA) detectors: Transforming discoveries demand breakthrough technologies, Heliophys. 2050 White Pap. (2021) 4024.
[9] J. Goldstein, D.J. McComas, The big picture: Imaging of the global geospace environment by the TWINS mission, Rev. Geophys. 56 (2018) 251.
[10] H.O. Funsten, et al., The interstellar boundary explorer high energy (IBEX-Hi) neutral atom imager, Space Sci. Rev. 146 (2009) 75.
[11] S.M. Krimigis, et al., Imaging the interaction of the heliosphere with the interstellar medium from Saturn with Cassini, Science 326 (5955) (2009) 971–973.
[12] C. Avanzini, et al., Characterization of a low-pressure micro-megas-like gaseous detector with low energy X-Ray sources, Nucl. Instrum. Methods Phys. Res. A 1045 (2023) 167592.
[13] G. Antonelli, et al., An innovative micro strip gas detector for low energy cosmic rays detection, PoS(ICRC2023) 167 (2023).
[14] Y. Giomataris, Ph. Rebourgeard, J.P. Robert, G. Charpak, MICROMEGAS: A high-granularity position-sensitive gaseous detector for high particle-flux environments, Nucl. Instrum. Methods Phys. Res. A 376 (1996) 29–35.
[15] I. Giomataris, et al., Micromegas in a bulk, Nucl. Instrum. Methods Phys. Res. A 560 (2006) 405–408.
[16] T. Alexopoulos, et al., Development of large size micromegas detector for the upgrade of the ATLAS muon system, Nucl. Instrum. Methods Phys. Res. A 617 (2010) 161–165.
[17] F. Kuger, et al., Mesh geometry impact on micromegas performance with an exchangeable mesh prototype, Nucl. Instrum. Methods Phys. Res. A 824 (2016) 541–542.
[18] ISO 20485:2017-11 (2017), Non-Destructive Testing - Leak Testing - Tracer Gas Method, Standard, International Organization for Standardization, Geneva, CH.
[19] C. Avanzini, et al., Charge sensitive preamplifier design optimization for low-pressure Micro-Megas gaseous detector operations, Nucl. Instrum. Methods Phys. Res. A 1048 (2023) 167915.
[20] Fabio Sauli, Book Gaseous Radiation Detectors, 2002.
[21] H. Bichsel, D.H. Peirson, J.W. Boring, A. Green, M. Inokuti, G. Hurst, W values for gases: Experimental data and suggested values, Rep. Int. Comm. Radiat. Units Meas. os-16 (2) (1979) 18–32.
[22] S. Roesler, M. Silari, PDG, commonly used radiative sources, downloadable PDF file at https://pdg.lbl.gov/2023/reviews/rpp2022-rev-commonly-used-radioactive-sources.pdf.
[23] R. Veenhof, Photon detection in a gas, Nucl. Instrum. Methods Phys. Res. A 563 (2006) 291–298.
[24] S. Agostinelli, et al., Geant4—A simulation toolkit, Nucl. Instrum. Methods Phys. Res. A 506 (2003) 250–303.
[25] R. Veenhof, The software homepage available at https://garfieldpp.web.cern.ch/garfieldpp.
[26] S. Biagi, Transport of electrons in gas mixtures, software source files avaialable at http://degrad.web.cern.ch/degrad/.
[27] R. Brun, F. Rademakers, ROOT - An object oriented data analysis framework, proceedings AIHENP'96 workshop, Lausanne, Sep. 1996, Nucl. Instrum. Methods Phys. Res. A 389 (1997) 81–86.
[28] M. Iodice, Performance studies of MicroMegas for the ATLAS experiment, JINST 9 (2014) C01017.
[29] K. Nikolopoulos, P. Bhattacharya, V. Chernyatin, R. Veenhof, Electron transparency of a micromegas mesh, JINST 6 (2011) P06011.
[30] Ö. Şahin, İ. Tapan, R. Veenhof, Secondary avalanches in gas mixtures, Nucl. Instrum. Methods Phys. Res. A 718 (2013) 432–433.